Mixed mode oscillations as a mechanism for pseudo-plateau bursting

**Theodore Vo · Richard Bertram · Joel Tabak ·
Martin Wechselberger**

Abstract We combine bifurcation analysis with the theory of canard-induced mixed mode oscillations to investigate the dynamics of a novel form of bursting. This bursting oscillation, which arises from a model of the electrical activity of a pituitary cell, is characterized by small impulses or spikes riding on top of an elevated voltage plateau. Oscillations with these characteristics have been called "pseudo-plateau bursting". Unlike standard bursting, the subsystem of fast variables does not possess a stable branch of periodic spiking solutions, and in the case studied here the standard fast/slow analysis provides little information about the underlying dynamics. We demonstrate that the bursting is actually a canard-induced mixed mode oscillation, and use canard theory to characterize the dynamics of the oscillation. We also use bifurcation analysis of the full system of equations to extend the results of the singular analysis to the physiological regime. This demonstrates that the combination of these two analysis techniques can be a powerful tool for understanding the pseudo-plateau bursting oscillations that arise in electrically excitable pituitary cells and isolated pancreatic β-cells.

Keywords Pseudo-plateau burst · Pituitary cell ·
Conductance-based model · Mixed mode oscillation ·
Canard · Slow-fast system · Bifurcation analysis

1 Introduction

Electrical bursting is characterized by episodes of electrical impulses followed by periods of quiescence during which the cell is repolarized. These oscillations are often observed in nerve and endocrine cells, and have been the focus of mathematical modeling and analysis. Many hormone-secreting cells in the anterior pituitary gland, such as lactotrophs, somatotrophs, and corticotrophs, exhibit fast bursting with small spikes arising from an elevated or depolarized voltage (Kuryshev et al. 1996; Van Goor et al. 2001). Single pancreatic β-cells, isolated from islets, exhibit a similar type of bursting pattern (Kinard et al. 1999). Figure 1(a) shows an example from a pituitary lactotroph cell line (GH4 cell). Mathematical models for bursting in lactotrophs (Tabak et al. 2007; Toporikova et al. 2008), somatotrophs (Tsaneva-Atanasova et al. 2007), corticotrophs (LeBeau et al. 1998; Shorten et al. 2000), and single β-cells (Zhang et al. 2003) have been developed and analyzed. This type of bursting, called "pseudo-plateau" bursting, is quite different from that of most neurons and neuron models, as discussed in Stern (2008).

We recently described a model that is unlike other models of pseudo-plateau bursting in that the bursting persists almost unaltered when the variable for the
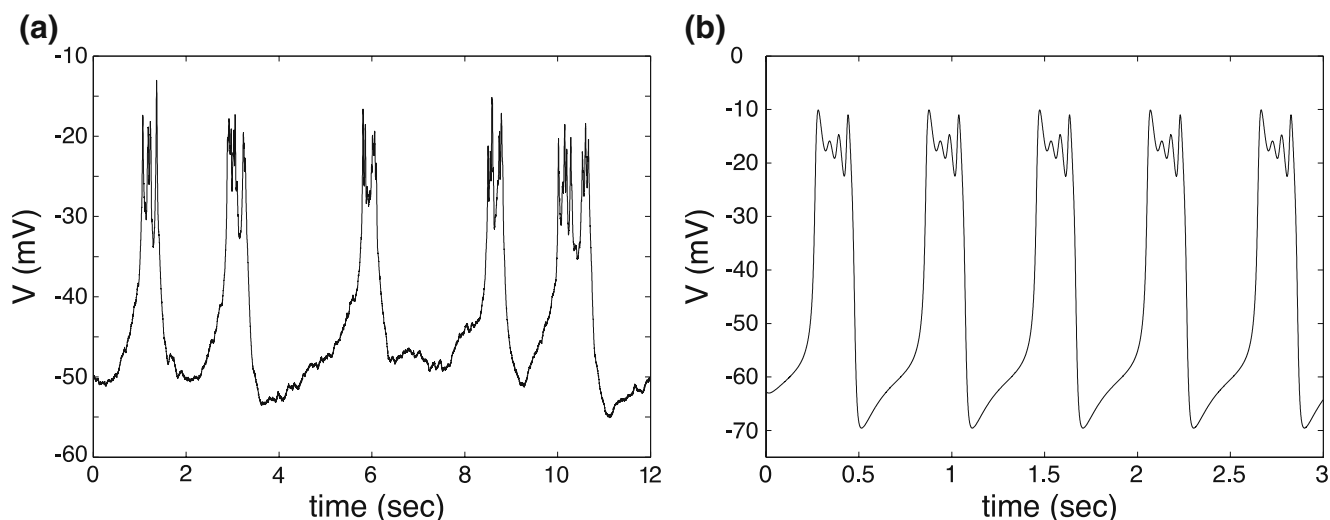
T. Vo · M. Wechselberger (✉)
School of Mathematics and Statistics,
University of Sydney, Sydney, NSW, Australia
e-mail: wm@maths.usyd.edu.au

R. Bertram
Department of Mathematics and Programs in Neuroscience
and Molecular Biophysics, Florida State University,
Tallahassee, FL, USA

J. Tabak
Department of Biological Science, Florida State University,
Tallahassee, FL, USA

(a)

(b)

Fig. 1 (**a**) Perforated patch electrical recording of bursting in a GH4 pituitary cell. (**b**) Bursting produced by the model with the default parameters shown in Table 1, with $C = 6$ pF, $g_K = 4.4$ nS, and $g_A = 18$ nS

intracellular Ca^{2+} concentration is fixed or eliminated (Toporikova et al. 2008). This is unusual, since the slow variation of the intracellular Ca^{2+} concentration is typically responsible for clustering impulses into periodic episodes of activity. Previously, we analyzed some of the properties of this unusual form of bursting (Toporikova et al. 2008). In the current article we extend this in two ways. First, we show how the bursting is situated in parameter space relative to other types of behaviors, and demonstrate how the number of spikes per burst varies in parameter space. Second, we take advantage of the different time scales within this model to analyze the mechanism for the bursting. We show that the bursting is actually a canard-induced mixed mode oscillation (MMO) where a MMO pattern corresponds to a switching between small-amplitude oscillations and large relaxation oscillations. Using geometric singular perturbation analysis (Fenichel 1979; Jones 1995; Wechselberger 2005; Brons et al. 2006), we demonstrate the origin of the MMO, identify the region in parameter space where the MMO exists, and show how the number of small amplitude oscillations (or spikes) varies in parameter space. In so doing, we identify the mechanism for this type of pseudo-plateau bursting, and also perform analyses at the singular limit to explain behaviors seen away from this limit. Mixed mode oscillations have been described previously for neural models and data (Erchova and McGonigle 2008; Wechselberger 2005; Rubin and Wechselberger 2007; Rotstein et al. 2008; Ermentrout and Wechselberger 2009; Drover et al. 2005; Brons et al. 2008; Krupa et al. 2008; Guckenheimer et al. 1997), but this is the first example where the MMOs form bursting oscillations.

2 The mathematical model

The model is a minimal description of the electrical activity and Ca^{2+} dynamics in a pituitary lactotroph (Toporikova et al. 2008). This is based on another model (Tabak et al. 2007), which produces bursting over a range of parameter values. For much of this range the bursting is driven by slow activity-dependent variation in the Ca^{2+} concentration. However, for a subset of this range the Ca^{2+} concentration can be clamped and bursting persists. In the model by Toporikova et al. this latter form of bursting was examined, and the Ca^{2+} variable removed, since variation in Ca^{2+} was not necessary to produce the bursting. This is the model we use here.

The model includes variables for the membrane potential (V) of the cell, the fraction of activated K^+ channels of the delayed rectifier type (n), and the fraction of A-type K^+ channels that are not inactivated (e). The differential equations are

$$C\frac{dV}{dt} = -(I_{Ca} + I_K + I_A + I_L) \quad (2.1)$$

$$\tau_e\frac{de}{dt} = e_\infty(V) - e \quad (2.2)$$

$$\tau_n\frac{dn}{dt} = n_\infty(V) - n \quad (2.3)$$

where I_{Ca} is an inward Ca^{2+} current and all other currents are outward K^+ currents. I_K is a delayed rectifier current, I_A is an A-type current that inactivates when V is elevated, and I_L is a constant-conductance

current that replaces the Ca^{2+}-activated K^+ current in the lactotroph model of Tabak et al. (2007). The ionic currents are given by

$$I_{Ca} = g_{Ca} m_\infty(V)(V - V_{Ca}) \qquad (2.4)$$

$$I_K = g_K n(V - V_K) \qquad (2.5)$$

$$I_A = g_A a_\infty(V) e(V - V_K) \qquad (2.6)$$

$$I_L = g_L(V - V_K) \ . \qquad (2.7)$$

The activation of the Ca^{2+} current and the A-type K^+ current is very fast, and is modeled as instantaneous, with steady-state activation functions $m_\infty(V)$ and $a_\infty(V)$. Mathematically, this can be justified by a center-manifold reduction (Rubin and Wechselberger 2007). The delayed rectifier current activates more slowly, with activation dynamics given by Eq. (2.3), and the A-type current also inactivates relatively slowly, with inactivation dynamics given by Eq. (2.2). Without I_A this is just the well-known Morris–Lecar model (Morris and Lecar 1981), a minimal biophysical model for membrane excitability that is capable of producing impulses, but not bursts of impulses.

Steady state activation functions have the form

$$x_\infty(V) = \frac{1}{1 + \exp\left(\frac{V_x - V}{s_x}\right)} \qquad (2.8)$$

for $x = m, n, a$, while the inactivation function is

$$e_\infty(V) = \frac{1}{1 + \exp\left(\frac{V - V_e}{s_e}\right)} \ . \qquad (2.9)$$

System parameters are: time constants (τ_n and τ_e), membrane capacitance C, current conductances (g_{Ca}, g_K, g_A, g_L), Nernst potentials (V_{Ca} and V_K), and shape parameters for the steady state functions (V_m, V_n, V_a, V_e, s_m, s_n, s_a, s_e). Values are given in Table 1.

Numerical simulations were performed with the fourth-order Runge–Kutta integration method, as implemented in the XPPAUT software package (Ermentrout 2002). Computer codes are freely available online at www.math.fsu.edu/~bertram/software/pituitary. Bifurcation diagrams and phase portraits of the singular perturbation analysis were also computed using XPPAUT. All graphics were produced with the software package MATLAB.

Figure 1(b) shows bursting oscillations produced by the model. Notice the small spikes that occur on top of a depolarized voltage plateau, which is characteristic of the bursting that often occurs in lactotrophs, somatotrophs, corticotrophs, and isolated β-cells. The

Table 1 Parameter values used in the model

Parameter	Value	Definition
C	0–20 pF	Membrane capacitance
g_K	0–10 nS	Maximal conductance of delayed rectifier K^+ channels
g_A	0–25 nS	Maximal conductance of A-type K^+ channels
g_{Ca}	2 nS	Maximal conductance of Ca^{2+} channels
V_{Ca}	50 mV	Reversal potential for Ca^{2+}
V_m	−20 mV	Voltage value at midpoint of m_∞
s_m	12 mV	Slope parameter of m_∞
V_K	−75 mV	Reversal potential for K^+
V_n	−5 mV	Voltage value at midpoint of n_∞
s_n	10 mV	Slope parameter of n_∞
τ_n	40 ms	Time constant for n
V_a	−20 mV	Voltage value at midpoint of a_∞
s_a	10 mV	Slope parameter of a_∞
V_e	−60 mV	Voltage value at midpoint of e_∞
s_e	5 mV	Slope parameter of e_∞
g_L	0.3 nS	Maximal conductance of leak current
τ_e	20 ms	Time constant of e

bursting in the GH4 cell is very noisy, which is typical of pituitary bursting. In contrast, the model is deterministic, and thus the bursting is much more regular.

The three model variables vary on different time scales. The time scale for variation in V (τ_V) can be estimated by the ratio of the model cell capacitance C to the maximum ion channel conductance, $g_{max} = \max\{g_{Ca}, g_K, g_A, g_L\}$ (more precisely, one uses dimensional analysis to identify the different time scales; see later). In most of our analysis and simulations, $C = 2$ pF and $g_{max} > 2$ nS. Thus, $\tau_V = C/g_{max} < 1$ ms. (The capacitance value chosen is intermediate between the more common 5 pF of somatotrophs or 6 pF of lactotrophs and the singular limit. We later vary C to investigate how the behavior changes with changes in capacitance.) The time constants for the other variables are given explicitly as model parameters: $\tau_e = 20$ ms and $\tau_n = 40$ ms. Thus, the V variable changes rapidly and the e and n variables change on slower time scales. We take advantage of this separation of time scales, and increase the disparity further by reducing C, when we apply geometric singular perturbation analysis to the system.

3 Pseudo-plateau bursting boundaries in parameter space

Our goals here are to determine how pseudo-plateau bursting relates to other states of the system such as

tonic firing (spiking) or an equilibrium state (either hyperpolarized or depolarized) by changing three key model parameters, and to determine how the number of spikes within a bursting pattern varies with parameters. The three parameters that we vary are the maximum conductances of the delayed rectifier (g_K) and A-type K$^+$ currents (g_A), and the capacitance (C). The first parameter, g_K, was chosen since it controls the number of spikes per burst (as we discuss later). The second parameter, g_A, was varied in our previous analysis, where we showed that the A-type current is crucial for the bursting (Toporikova et al. 2008). The third parameter, C, sets the time scale for voltage ($\tau_V = C/g_{max}$), as discussed in the previous section. Decreasing C reduces τ_V and widens the separation of time scales between V and the slower variables n and e.

We begin by treating g_K as the bifurcation parameter, keeping the other two parameters fixed at $g_A = 2$ nS and $C = 2$ pF. Figure 2(a) is a bifurcation diagram


(a)

(b)
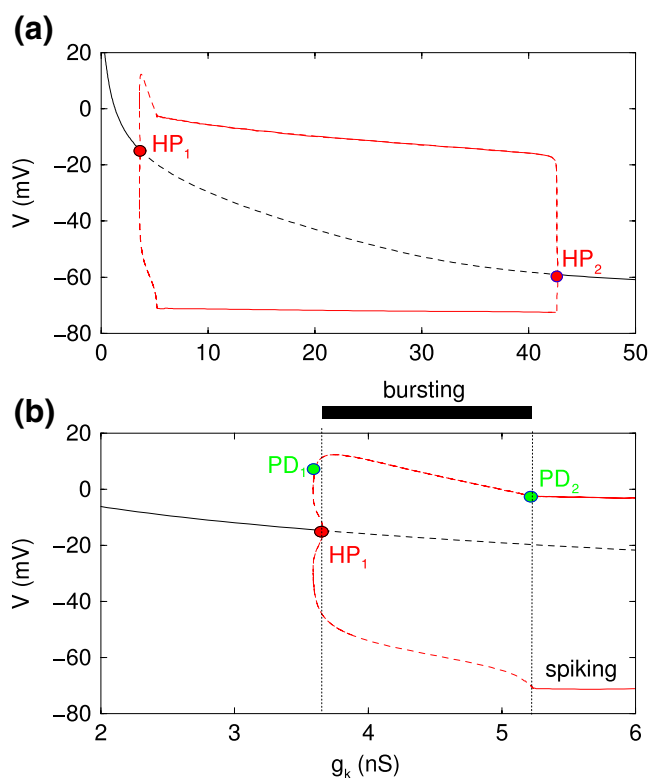
Fig. 2 (**a**) Bifurcation diagram illustrating the asymptotic dynamics of the system, with g_K as bifurcation parameter (fixed $C = 2$ and $g_A = 2$). Steady state solutions (*black*) are either stable (*solid*) or unstable (*dashed*). *Red* Minimum and maximum V of periodic spiking solutions, either stable (*solid*) or unstable (*dashed*). Subcritical Hopf bifurcations (HP$_1$, HP$_2$) initiate and terminate the periodic branch. (**b**) Blowup of the diagram in the *top panel* near HP$_1$, highlighting the region where bursting occurs. *PD* period doubling bifurcation

showing the asymptotic behavior of the system for a range of values of g_K. The black curve represents steady state solutions, which could be stable (solid curve) or unstable (dashed). The red curves represent the maximum and minimum voltages of periodic spiking solutions, which may be stable (solid) or unstable (dashed). For small values of g_K the steady state solutions are stable, and at an elevated or depolarized voltage. They lose stability at a subcritical Hopf bifurcation (HP$_1$), giving rise to a branch of periodic spiking solutions. The steady state solutions regain stability at another subcritical Hopf bifurcation (HP$_2$).

The spiking solutions are stable for most of the range of g_K for which they exist. However, as highlighted in Fig. 2(b), there is a small range of g_K values where the spiking branch is unstable. This is expected to the left of HP$_1$ and to the right of HP$_2$ because these Hopf bifurcations are subcritical. However, there is a much larger region to the right of HP$_1$ where the periodic solutions are unstable, and this is surprising. The explanation is that the spiking branch goes through a period doubling bifurcation (PD$_1$) shortly after turning around at a saddle-node of periodics (SNP, not labeled). The primary spiking branch regains stability only after a second PD bifurcation occurs (PD$_2$). Thus, between HP$_1$ and PD$_2$ the steady state and regular spiking branches are both unstable. This is the region where bursting occurs. We show later, by going to the singular limit $C \to 0$, that this bursting is a canard-induced mixed mode oscillation (see, e.g., Brons et al. 2006). The stable spiking solution that occurs between the left SNP bifurcation and PD$_1$ loses stability and is replaced by a stable doublet spiking solution at PD$_1$. We distinguish this from the bursting solution that occurs between PD$_1$ and PD$_2$.
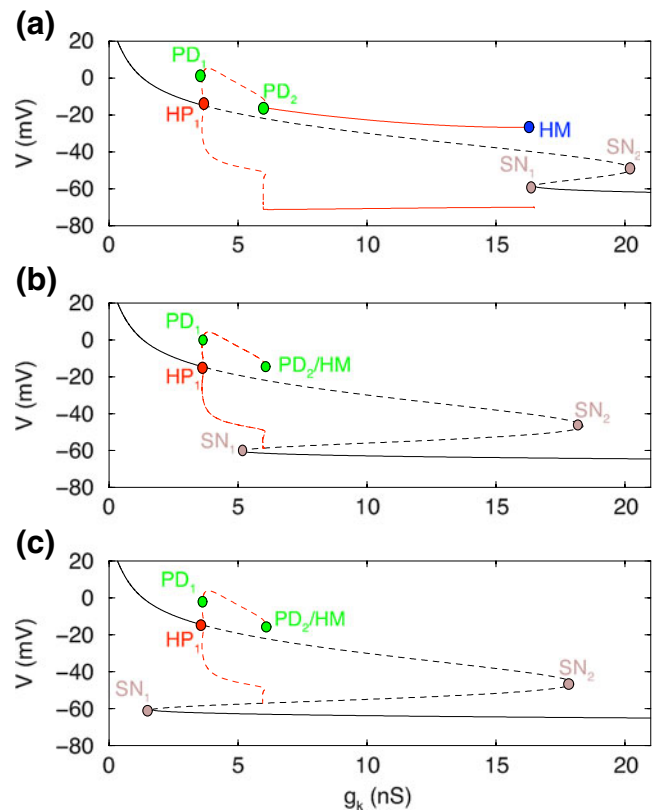
We next determine how the bifurcation points in Fig. 2 vary when the conductance g_A of the I_A current is changed. This is done since our prior analysis showed the importance of I_A in the production of bursting. We use a two-parameter (g_K, g_A) diagram to show the dependence of the different bifurcations on the g_K and g_A parameters (Fig. 3(a)). The left subcritical Hopf bifurcation of Fig. 2(a) is insensitive to g_A, because the A-type current is inactivated at depolarized voltages. Thus, the curve of bifurcation points of this type is nearly vertical in Fig. 3(a) (left green curve). On the other hand, the right subcritical Hopf bifurcation in Fig. 2(a) is very sensitive to g_A because when g_A is greater, less g_K is needed to destabilize the hyperpolarized steady state (right red curve in Fig. 3(a)). The left PD bifurcation in Fig. 2(b) remains close to HP$_1$ as g_A is varied, so this bifurcation curve is almost indistinguishable from the HP$_1$ curve. Therefore, we only show
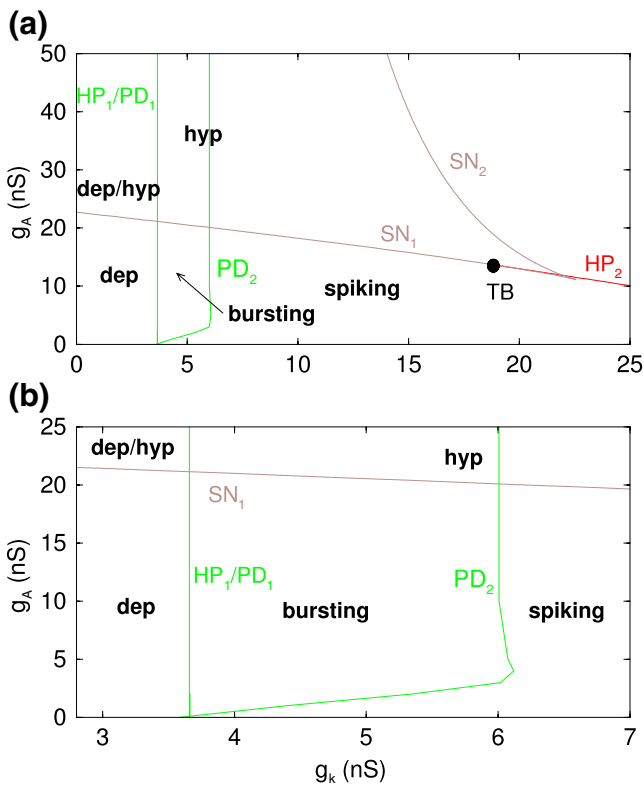
Fig. 3 (**a**) Two-parameter bifurcation diagram in the parameters g_K and g_A, with $C = 2$ pF. (**b**) Blowup of panel **a**, highlighting the bursting region. The label SN represents a saddle node bifurcation. The label TB represents a codimension-2 Takens–Bogdanov bifurcation. The system behaviors are in *bold*: *bursting* periodic bursting, *dep* depolarized steady state, *hyp* hyperpolarized steady state, *dep/hyp* bistable region

Fig. 4 (**a**) One-parameter bifurcation diagram for $C = 2$ pF and $g_A = 15$ nS. There is a fold in the stationary branch, with two saddle-node (SN) bifurcations. The stable spiking branch terminates at a homoclinic (HM) saddle-node on invariant *circle* bifurcation. Bursting exists between PD_1 and PD_2. (**b**) Increasing g_A to 20.5 pS moves SN_1 to the left of PD_2. The unstable spiking branch terminates at a homoclinic saddle-node loop bifurcation that is very close to PD_2. Bursting only exists between PD_1 and SN_1. (**c**) Further increasing g_A to 22 nS moves SN_1 to the *left* of PD_1, so that bursting is no longer produced

a single curve in the figure and denote it by HP_1/PD_1. The PD_2 bifurcation in Fig. 2(b) is important as the right boundary for the bursting. For small values of g_A, PD_2 moves to the right as g_A is increased, increasing the range over which bursting occurs. However, when g_A becomes sufficiently large the PD bifurcation becomes insensitive to further increases. As a result, the PD_2 curve in Fig. 3(a) first has a positive slope, but eventually becomes vertical. The HP_1/PD_1 and PD_2 curves then form the left, right, and lower boundaries of the region of bursting (Fig. 3). The lower boundary clearly shows that the I_A current is necessary for bursting in this model (independent of the strength of the delayed rectifier).

To see where the upper boundary of the bursting region (the SN_1 branch) comes from, we return to a one-parameter bifurcation diagram, but this time with a larger g_A conductance, $g_A = 15$ nS (Fig. 4(a)). With this larger g_A the stationary branch of solutions is folded, creating the two knees or saddle-node (SN)

bifurcations in Fig. 4(a). The periodic spiking branch that emerges from the Hopf bifurcation (HP_1) goes through two PD bifurcations as before, gaining stability at the right PD. The stabilized spiking branch now terminates at a homoclinic saddle-node on invariant circle bifurcation (labeled HM in the figure). This SNIC bifurcation comes about when HP_2 from Figs. 2 and 3 coalesces with the lower SN (SN_1) in Fig. 4(a) at a codimension-2 Takens–Bogdanov (TB) bifurcation.

When g_A is increased further SN_1 shifts leftward, eventually moving to the left of PD_2. As this happens, PD_2 and HM move together, eliminating the stable branch of spiking solutions (Fig. 4(b)). The interval of bursting solutions now terminates at SN_1, rather than PD_2, and the termination is through a homoclinic bifurcation; the silent phase of the burst gets progressively longer as g_K approaches the SN_1 bifurcation. When g_A

is increased even further SN_1 moves to the left of PD_1, eliminating the interval of bursting solutions (Fig. 4(c)). Thus the stable asymptotic structure of the system is a depolarized and/or a hyperpolarized steady state, for the full range of g_K.

The sequence of events described above is summarized in the two-parameter (g_K, g_A) diagram (Fig. 3). The two branches of SN bifurcations (the left and right knees) are shown in brown in panel A, coalescing at a codimension-2 cusp bifurcation. The HP_2 bifurcation coalesces with the SN_1 bifurcation at the labeled TB point. For all g_A values above this point the spiking branch terminates at a homoclinic bifurcation (a SNIC bifurcation for lower g_A values and a saddle-loop bifurcation for higher g_A values; see Fig. 4). The SN_1 bifurcation branch forms the upper boundary for the bursting, since for all g_A values above this curve the system is either globally stable with a hyperpolarized stationary attractor, or bistable with hyperpolarized and depolarized stationary attractors. This loss of bursting oscillations for sufficiently large g_A was described previously (Toporikova et al. 2008), but not in terms of the (g_K, g_A) bifurcation structure. This (g_K, g_A) diagram provides the curves that delimit the various system behaviors which are given in bold text in Fig. 3.

Varying the g_A parameter, as was done above, varies the influence that the important A-type K^+ current has on the system. We next vary the membrane capacitance C, which changes the time scale separation between V and the slower variables e and n. Making C larger makes V slower, thereby decreasing the time scale separation. Figure 5(a) is a two-parameter bifurcation diagram showing how the locations of the subcritical Hopf bifurcations vary with C and g_K. This is done for four different values of g_A. In all cases, as C is increased the HP bifurcations come together, eventually coalescing at a relatively high C value. Beyond this value, the system is steady, exhibiting neither continuous spiking nor bursting oscillations.

From Fig. 5(a) it is clear that the left branch of the HP curve is unaffected by changes in g_A over the range $g_A \in [1, 5]$ nS, so in the blowup figure in panel B the left branch of a single HP curve is shown. Also shown, for four values of g_A, are branches of PD bifurcations. For each value of g_A, bursting exists between the HP_1 curve and the PD_2 curve. Between the PD_1 branch and the HP_1 curve a stable hyperpolarized stationary solution coexists with a spike doublet solution (the doublet bifurcates further through a series of PD bifurcations, leading ultimately to chaos). We see that the bursting region expands as g_A is increased, at least for g_A up to 5 nS, and that the bursting region also expands as C decreases (except for a minor decrease of the bursting
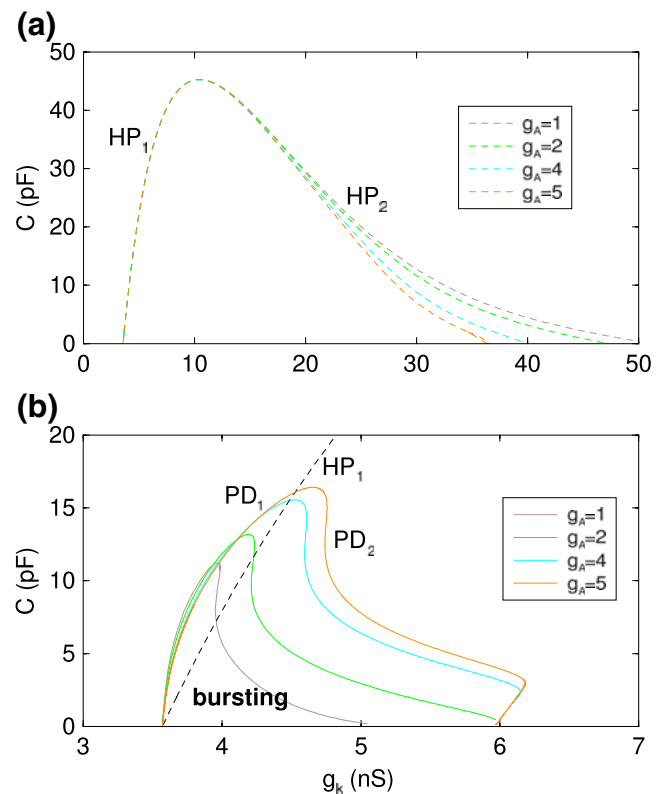
Fig. 5 (**a**) Two-parameter bifurcation diagram illustrating the dependence of the Hopf bifurcations on the membrane capacitance C for four different values of g_A. The HP_1 bifurcation is insensitive to g_A. (**b**) Two-parameter bifurcation diagram illustrating the C dependence of period doubling bifurcations of the primary spiking solution. A single HP_1 curve is also included. Bursting occurs between HP_1 and PD_2. Between PD_1 and HP_1 the system is bistable between a hyperpolarized steady state and a complex spiking pattern (doublets, four-spike pattern, etc.)

regime in the limit $C \to 0$ for g_A greater than 1 nS). We also point out that, in the limit $C \to 0$, the range of g_K values for which bursting occurs extends from HP_1 to $g_K \approx 6$ nS for the larger values of g_A. We show this again later in our analysis of the mixed mode oscillations that underlie bursting in this system.

We next demonstrate how the number of spikes per burst varies. This is an important biological feature, since this number (partly) determines the burst duration (active phase) and hence the amount of Ca^{2+} influx, and thus the amount of hormone released from a cell. We set $g_A = 4$ nS and vary g_K and C over a rectangular grid of values, with $\Delta g_K = 0.1$ nS and $\Delta C = 1$ pF. For each choice of parameters we solve the differential equations numerically and count the number of spikes per burst. In Fig. 6 circles represent the number of spikes in a burst. Large reddish circles represent bursts with many spikes (maximum of 62 for
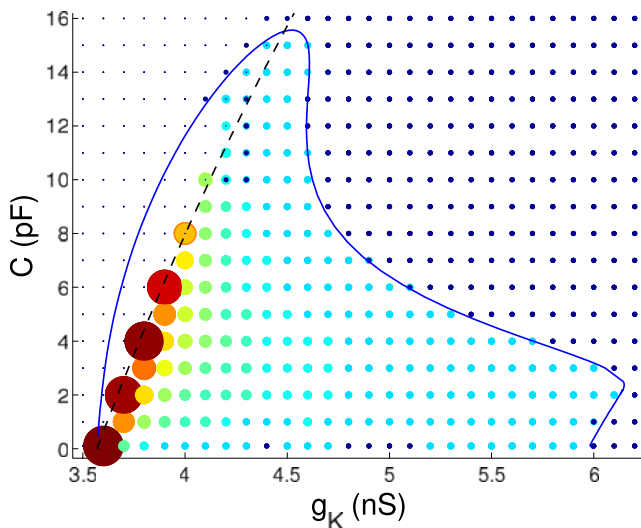
Fig. 6 Number of spikes per burst for a grid of g_K and C values ($g_A = 4$ nS). *Single points* represent steady states, and *small dark circles* represent continuous spiking. *Larger circles with colors* ranging from *light blue* to *red* represent bursting. The larger the *circle*, the greater the number of spikes per burst. The minimum number of spikes is 2 (small, *light blue*), and the maximum is 62 (large, *red*). *Circles with points in the middle* represent bistable dynamics

the largest circles), while small blue circles represent bursts with few spikes (minimum of 2). We superimpose the PD curve for $g_A = 4$ nS and the HP_1 curve onto the grid. To the right of PD_2 the system exhibits continuous spiking, represented by small dark circles. To the left and above the PD_1 branch the system is at a steady state (represented by points). Bursting or complex spiking (doublets, four-spike patterns bifurcating off of the doublets branch, etc.) occurs only within the two branches of the PD curve. Between the PD_1 and HP_1 curves the system is bistable, with coexisting stable hyperpolarized steady states and simple or complex spiking (the bistable region extends to the left of the PD_1 bifurcation to the saddle node of periodics (SNP); see discussion of Fig. 2). Thus, in the simulation grid this region is occupied by a mix of points (steady states) and circles (simple or complex spiking). For some parameter values there are circles with points in the middle, representing bistable solutions that were found by varying the initial conditions. In many cases only one stable solution was found, which maybe be due to a small basin of attraction of the other stable solution. The most important observation to make from Fig. 6 is that the number of spikes per burst is greatest at the lower g_K values. We show later that this is predicted from the analysis of mixed mode oscillations in the $C \to 0$ limit.

4 Geometric singular perturbation analysis

We now show the origin of the spiking and bursting oscillations described in previous sections. The bursting oscillations are not of the standard type, which are due to bistability of the fast subsystem of variables between a hyperpolarized steady state and a periodic (spiking) solution (Rinzel 1987; Rinzel and Ermentrout 1998). To understand the bursts produced by the current model we take advantage of the time-scale separation of the variables that was pointed out in Section 2.

To rigorously justify the time-scale separation in (Eqs. (2.1)–(2.3)), we nondimensionalize the system by introducing a dimensionless 'voltage' variable $v = V/k_v$ where we choose $k_v = 100$ mV as a typical voltage scale, and a dimensionless 'time' variable $\tau = t/k_t$ where $k_t = \tau_e = 20$ ms is a typical (slow) time scale of the system. This leads to the dimensionless form

$$\frac{dv}{d\tau} = \frac{k_t}{\tau_v} f(e, n, v)$$

$$\frac{dn}{d\tau} = \frac{k_t}{\tau_n} (n_\infty(v) - n)$$

$$\frac{de}{d\tau} = \frac{k_t}{\tau_e} (e_\infty(v) - e) \tag{4.1}$$

where

$$f(e, n, v) \equiv -\big\{ \bar{g}_{Ca} m_\infty (v - \bar{V}_{Ca}) \\ + (\bar{g}_K n + \bar{g}_A a_\infty e + \bar{g}_L)(v - \bar{V}_K) \big\} \tag{4.2}$$

and $\tau_v = C/g_{max}$. Note that the overbar denotes a dimensionless parameter. The right hand sides take the form of a scaling factor multiplied by some quantity which is $O(1)$. With the choice of the above scaling factors k_v and k_t, we see that the dynamics of the variables (n, e) are of $O(1)$ while the dynamics of the variable v is $O(1/\varepsilon)$ where

$$\varepsilon \equiv \frac{\tau_v}{k_t} = \frac{C}{k_t g_{max}} \ll 1. \tag{4.3}$$

In particular, decreasing the capacitance C decreases ε and hence increases the time scale separation between the dynamics of the fast variable v and the slow variables (n, e). Therefore, system (4.1) is a singularly perturbed system with two slow variables (n, e), one fast variable (v) and singular perturbation parameter ε.

The dimensional analysis above demonstrates that the original system (Eqs. (2.1)–(2.3)) already has the correct factorization (although in dimensional form). Hence, for easier comparison with the bifurcation analysis presented in Section 2, we use this original system in our analysis and treat V as a fast variable, (e, n)

as slow variables and C as the singular perturbation parameter.

We begin our geometric singular perturbation analysis by moving to the singular limit, $C \to 0$, where V changes instantaneously and the slow variables evolve in (slow) time according to (Eqs. (2.2)–(2.3)). If we define the right hand side of Eq. (2.1) by

$$g_{max} \, f(V, e, n) \equiv -(I_{Ca} + I_K + I_A + I_L) \ , \tag{4.4}$$

then $f(V, e, n) = 0$ defines the corresponding quasi-steady state condition due to the instantaneous dynamics of V. The two slow variables (e, n) evolve in (slow) time so that this condition is satisfied. That is, the phase point in $\mathbb{R}^3$ travels along the *critical manifold*

$$S \equiv \{(V, e, n) \in \mathbb{R}^3 : \, f(V, e, n) = 0\} \tag{4.5}$$

(except at discrete jumps from one sheet of the manifold to another which are controlled by the layer problem, defined below). This slow evolution on S is called the *reduced flow*. The implicit equation $f = 0$ can be solved explicitly for n (or for e, but not V), which enters into I_K (and f) linearly,

$$n = n(e, V) = -\frac{1}{g_K} \left[g_{Ca} m_\infty(V) \frac{(V - V_{Ca})}{(V - V_K)} \right. $$
$$\left. + g_A a_\infty(V) e + g_L \right] \ . \tag{4.6}$$

The critical manifold S is a folded surface, shown in Fig. 7(a) for one set of g_K and g_A values. The bottom, middle, and top sheets of the surface are separated by fold curves (in red). Fold curve L^- separates the bottom and middle sheets, while fold curve L^+ separates the middle and top sheets. Note that this geometric structure of the critical manifold will not change under the variation of g_K (it is only a scaling factor).

Since the critical manifold Eq. (4.6) is a graph over the base (e, V), the dynamics on the critical manifold, the reduced flow, can be described by the differential equation for e (Eq. (2.2)) and by differentiating $f(V, e, n) = 0$ with respect to time to obtain a differential equation for V. Thus,

$$\frac{d}{dt} f(V, e, n) = \frac{d}{dt} 0 \tag{4.7}$$

yields

$$-\frac{\partial f}{\partial V} \frac{dV}{dt} = \frac{\partial f}{\partial e} \frac{de}{dt} + \frac{\partial f}{\partial n} \frac{dn}{dt} \tag{4.8}$$

where $n = n(e, V)$ and the reduced system projected onto the base (e, V) is given by

$$-\frac{\partial f}{\partial V} \frac{dV}{dt} = \left(\frac{e_\infty - e}{\tau_e} \right) \frac{\partial f}{\partial e} + \left(\frac{n_\infty - n}{\tau_n} \right) \frac{\partial f}{\partial n} \tag{4.9}$$

$$\frac{de}{dt} = \left(\frac{e_\infty - e}{\tau_e} \right) \ . \tag{4.10}$$

This system is singular along the fold curves $L^\pm$, where $\frac{\partial f}{\partial V} = 0$. To remove this singularity we rescale time with the transformation $\tau \equiv -(\frac{\partial f}{\partial V})^{-1} t$. With this transformation we obtain the *desingularized system*:

$$\frac{dV}{d\tau} = \left(\frac{e_\infty - e}{\tau_e} \right) \frac{\partial f}{\partial e} + \left(\frac{n_\infty - n}{\tau_n} \right) \frac{\partial f}{\partial n} \equiv F(V, e, n) \tag{4.11}$$

$$\frac{de}{d\tau} = -\left(\frac{e_\infty - e}{\tau_e} \right) \frac{\partial f}{\partial V} \ . \tag{4.12}$$

The phase portraits of the reduced system and the desingularized system are equivalent on the top and bottom sheet of the critical manifold. Because of the time rescaling, the flow of the desingularized system on the middle sheet, where $\frac{\partial f}{\partial V} > 0$, must be reversed to obtain the equivalent reduced flow on the middle sheet. Thus the reduced flow can be obtained by analyzing the desingularized system.

The reduced flow, calculated by numerically solving Eqs. (4.11), (4.12), is shown on the critical manifold in Fig. 7(a) and its projection onto the e-V plane is shown in Fig. 7(b) (black curve, single arrow). The trajectory moves along the bottom sheet until it reaches L^-. At this point, the reduced flow is singular ($\frac{\partial f}{\partial V} = 0$) and the solution ceases to exist due to finite time blow-up. The quasi-steady state assumption $f = 0$ cannot hold anymore and we expect a rapid motion away from the fold-curve L^-. This rapid motion can be understood by switching to a fast (dimensionless) time scale $t_1 = t/\tau_v$ which transforms (Eqs. (2.1)–(2.3)) to

$$\frac{dV}{dt_1} = f(V, e, n) \tag{4.13}$$

$$\frac{de}{dt_1} = \frac{\tau_v}{\tau_e} (e_\infty(V) - e) \tag{4.14}$$
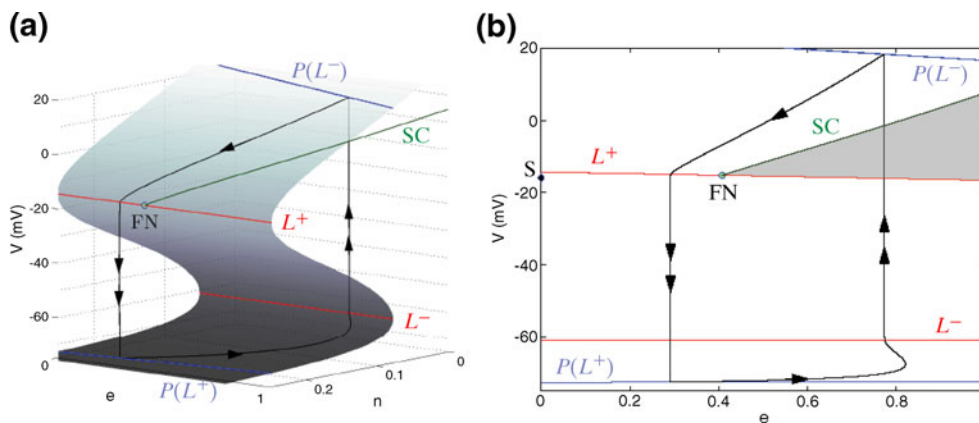
$$\frac{dn}{dt_1} = \frac{\tau_v}{\tau_n} (n_\infty(V) - n) \ . \tag{4.15}$$

Taking the singular limit $C \to 0$ we obtain the *layer problem*

$$\frac{dV}{dt_1} = f(V, e, n) \tag{4.16}$$

$$\frac{de}{dt_1} = \frac{dn}{dt_1} = 0 \tag{4.17}$$

Fig. 7 A singular periodic orbit (*black*) concatenated by slow and fast segments of the two singular limit systems, the reduced problem (4.11)–(4.12) and the layer problem (4.16)–(4.17), that leads to relaxation oscillations in (Eqs. (2.1)–(2.3)) for $C > 0$. Here, the periodic orbit does not enter the singular funnel of the folded node FN, bounded by the fold curve L^+ and the strong singular canard SC. (**a**) A view of the singular periodic orbit (*black*) and the critical manifold. (**b**) Projection onto the (e, V)-plane with the singular funnel highlighted in *gray*. FN is at $(e, V) = (0.41, -15.26)$, eigenvalue ratio is $\mu \approx 0.1$ and parameter values are $g_A = 0.2$ nS and $g_K = 4.0$ nS. There is also a saddle equilibrium S (*black diamond*) at $(e, V) = (1.5 \times 10^{-4}, -15.94)$

which describes the evolution of the fast variable V along one-dimensional fibers where (e, n) are constant parameters. Note that the critical manifold is the manifold of equilibria for the layer problem. The stability of these equilibria is determined by the sign of $\frac{\partial f}{\partial V}$. It follows that the lower and upper sheets, which we denote by $S_a^\pm$, are attracting ($\frac{\partial f}{\partial V} < 0$) while the middle sheet, denoted by S_r, is repelling ($\frac{\partial f}{\partial V} > 0$).

Going back to Fig. 7, we concatenate the trajectory of the reduced flow that reaches the fold-curve L^- with a fast fiber segment of (Eq. (4.16)–(4.17)) which provides the rapid motion from L^- to the stable top sheet S_a^+ (black curve, double arrow) at a point on $P(L^-)$. The curve $P(L^-)$ denotes the projection of L^- along fast fibers onto the stable top sheet S_a^+, while L^+ is projected onto the stable bottom sheet S_a^- as $P(L^+)$ (blue curves). From here the trajectory moves according to the reduced flow along the top sheet S_a^+ until L^+ is reached and the layer problem is again solved for the rapid motion to the stable bottom sheet S_a^- at a point on $P(L^+)$. Here, this concatenation of slow and fast segments leads to a singular periodic orbit. Geometric singular perturbation theory (Szmolyan and Wechselberger 2004) shows that this orbit perturbs to a nearby periodic relaxation oscillation orbit of system (Eqs. (2.1)–(2.3)) for sufficiently small $C \neq 0$. This relaxation oscillation orbit corresponds to a spiking solution below the PD_2 curve in Fig. 3. In the following, we apply geometric singular perturbation techniques to uncover the genesis of the bursting mechanism in system (Eqs. (2.1)–(2.3)).

5 Mixed mode oscillations

Mixed mode oscillations consist of small amplitude oscillations followed by large relaxation-type excursions, repeated periodically. An understanding of possible mechanisms for these oscillations using geometric singular perturbation theory has recently been achieved (Wechselberger 2005; Brøns et al. 2006; Guckenheimer 2008). One possibility is the existence of folded node singularities of the reduced flow together with an appropriate global return mechanism (see e.g., Brøns et al. 2006).

A folded singularity of the reduced system (Eqs. (4.9)–(4.10)) is an equilibrium of the desingularized system (Eqs. (4.11)–(4.12)) that occurs on a fold curve and satisfies

$$f(V, e, n) = 0 \tag{5.1}$$

$$F(V, e, n) = 0 \tag{5.2}$$

$$\frac{\partial f}{\partial V} = 0 \ . \tag{5.3}$$

Generically, this is different from an ordinary singularity of the reduced flow (an equilibrium), which is also an equilibrium of the desingularized flow but satisfies

$$f(V, e, n) = 0 \tag{5.4}$$

$$F(V, e, n) = 0 \tag{5.5}$$

$$\frac{\partial f}{\partial V} \neq 0 \ . \tag{5.6}$$

Such an ordinary equilibrium of the reduced flow is positioned away from the fold-curves $L^{\pm}$ and is also an equilibrium of the full system (Eqs. (2.1)–(2.3)), i.e.

$$f(V, e, n) = 0 \tag{5.7}$$

$$n = n_{\infty}(V) \tag{5.8}$$

$$e = e_{\infty}(V) \ . \tag{5.9}$$

These equilibria have been identified in the bifurcation diagrams of Section 2.

Linear stability analysis of a folded singularity indicates whether it is a folded node (FN), a folded saddle, or a folded focus. In the present case, and with parameter values $g_A = 4$ nS, $g_K = 4$ nS, a folded node singularity exists on the fold curve L^+ (shown in Fig. 8), since the eigenvalues of the linearization at the equilibrium point of the desingularized flow are both negative. Also, for this choice of parameter values the fold curves L^+ and L^- join and form a cusp-like structure near $e = 1$. Compare with Fig. 7 (where $g_A = 0.2$ nS and $g_K = 4$ nS) which also has a FN, but for which the fold curves do not form a cusp for e in the admissible range of $[0,1]$.

The reduced flow in the neighborhood of a folded node has very interesting properties. *Singular canards* (Benoit 1983; Szmolyan and Wechselberger 2001) exist in the neighborhood of a folded singularity. These trajectories enter the folded singularity, in our case along the top attracting sheet S_a^+ of the critical manifold, and move through the folded node singularity in finite time, emerging on the repelling middle sheet S_r and

traveling along it for some time. For folded nodes, this implies that there is a whole sector of singular canards, bounded below by L^+ and above by the strong singular canard (SC in Figs. 7 and 8) associated with the unique trajectory which is tangent to the eigendirection of the strong eigenvalue of the FN. This sector, the *singular funnel*, is shown in gray in Figs. 7 and 8. In the case of a folded saddle, only two such singular canards exist, while a folded focus has no singular canards.

For canard-induced MMOs to exist, a singularly perturbed system has to fulfill two major requirements (Brøns et al. 2006):

- The reduced flow has to possess a folded node singularity.
- There is a singular periodic orbit formed from the concatenation of slow and fast segments of the reduced and layer problems which starts with a fast fiber segment at the folded node singularity. This automatically assures that the global return of such a singular periodic orbit is within the singular funnel of the folded node.

If these two assumptions are fulfilled then canard theory implies that this singular periodic orbit perturbs to a nearby MMO orbit for sufficiently small $\varepsilon > 0$ ($C > 0$). In the case shown in Fig. 8, these assumptions are fulfilled; the singular periodic orbit starting at the FN indeed returns into the singular funnel. We therefore expect to find MMOs in system (Eqs. (2.1)–(2.3)). Furthermore, the theory predicts that the small amplitude oscillations of the MMO pattern occur in a
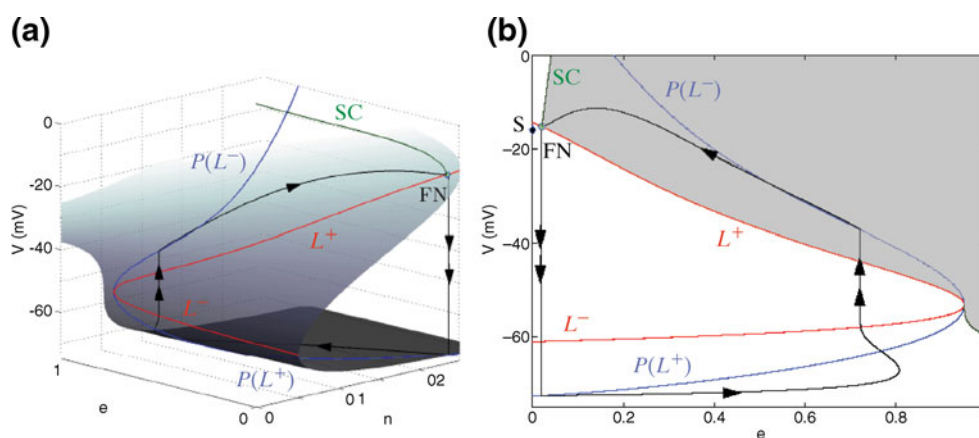

Fig. 8 A singular periodic orbit (*black*) concatenated by slow and fast segments of the two singular limit systems, the reduced problem (4.11)–(4.12) and the layer problem (4.16)–(4.17), that leads to MMO in (Eqs. (2.1)–(2.3)) for $C > 0$. Parameter values are $g_A = 4.0$ nS and $g_K = 4.0$ nS. (**a**) Critical manifold (surface) with fold curves L^- and L^+ (*red*) and fold curve projections $P(L^{\pm})$ (*blue*). Also shown is the strong singular canard (*green*, SC) of the folded node (FN). (**b**) Projection onto the (e, V)-plane with the singular funnel highlighted in *gray*. The FN is at $(e, V) = (0.02, -15.26)$ and has eigenvalue ratio of $\mu \approx 0.1$. There is also a saddle equilibrium S (*black diamond*) at $(e, V) = (1.4 \times 10^{-4}, -15.94)$

neighbourhood of the folded node and that the maximum amplitude of these small oscillations is $O(\sqrt{\varepsilon})$, i.e., the maximum amplitude grows proportional to the square root of the capacitance C. This also implies that the amplitude of the small oscillations vanishes in the singular limit $\varepsilon \to 0$ $(C \to 0)$.

The small amplitude oscillations are due to a geometric property of invariant manifolds near a folded node. According to Fenichel theory (Fenichel 1979; Jones 1995), the attracting and repelling sheets of the critical manifold ($S_a^\pm$ and S_r, respectively) away from the fold-curves $L^\pm$ perturb smoothly to locally invariant slow manifolds ($S_{a,C}^\pm$ and $S_{r,C}$, respectively) for C sufficiently small, but non-zero. These perturbed slow manifolds are in an $O(C)$ neighbourhood of the unperturbed critical manifolds. Furthermore, the flow on these perturbed slow manifolds is a smooth $O(C)$ perturbation of the reduced flow on the corresponding unperturbed manifolds. If one extends these perturbed slow manifolds by the flow into the vicinity of a folded node singularity, then the intersection of the attracting and repelling sheets is locally twisted (see Wechselberger 2005 for details; the numerical technique for computing twisted slow manifolds is described in Desroches et al. 2008.) Singular canards of the reduced flow perturb to actual canards of the original system. In our case, these canards follow $S_{a,c}^+$ toward the FN and $S_{r,c}$ afterwards before jumping to $S_{a,c}^-$. Since $S_{a,c}^+$ and $S_{r,c}$ are twisted near the FN, the canards rotate and produce the small spikes during the active phase of the burst.

Figure 9 confirms the predicted MMO result for $g_K = 4$ and $g_A = 4$. It illustrates the emergence of small amplitude oscillations in the voltage time course as C is increased. When $C = 0.05$ pF the (very) small amplitude oscillations are not yet visible. Projection of this trajectory onto (e, V)-space (not shown here) closely follows the singular periodic orbit in Fig. 8(b). When C is increased by a factor of 40 to $C = 2$ pF small oscillations appear near the end of the active phase; this is a bursting oscillation with small spikes (panel B). These reflect the rotational properties near the FN that were undetectable near the singular limit. When C is increased further to $C = 6$ pF the small oscillations are larger than before and occur throughout the active phase (panel C). Notice that in all three time courses the beginning of the active phase is characterized by a voltage peak. This is due to the shape of the critical manifold and the direction of the reduced flow, and is not one of the small oscillations associated with the folded node. For example, there are 8 small spikes associated with the FN in Fig. 9(c), preceded by an additional small spike. This additional oscillation does not
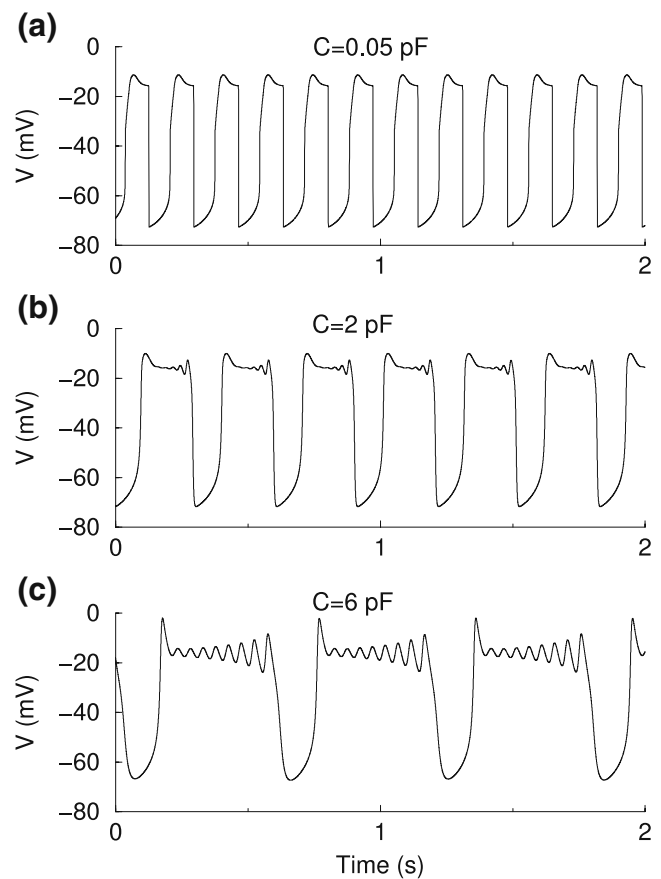
Fig. 9 Mixed mode oscillations with $g_K = 4$ nS, $g_A = 4$ nS, and various values of C. (**a**) $C = 0.05$ pF is very small and the small amplitude oscillations are not visible. (**b**) When C is increased 40-fold ($C = 2$ pF) small oscillations become visible during the active phase, reflecting the twists near the folded node. Here we find $s_{max} = 5$ plus one additional small oscillation at the beginning of the active phase. (**c**) With a larger capacitance, $C = 6$ pF, the small oscillations ($8 + 1$) occur throughout the active phase. The predicted maximum number $s_{max} = 5$ does not hold anymore because the capacitance C, considered as a singular perturbation parameter, is too large

vanish in the singular limit $C \to 0$, another indicator that it is not associated with the folded node.

For MMOs to exist, it is crucial that the phase point returns to the singular funnel of the folded node when entering the active phase of the oscillation. This will occur when the point on $P(L^-)$, that the phase point jumps to when leaving L^-, lies in the singular funnel of the folded node. If this does not happen, then no small oscillations will be produced and the trajectory will exhibit a relaxation oscillation. This is illustrated in Fig. 7, both on the critical manifold and on its projection onto the (e, V)-plane. In this example, there also exists a folded node, but since the projection curve $P(L^-)$ does not intersect the singular funnel (gray shaded

region in Fig. 7(b)) it follows that the return of the singular trajectory starting at the folded node is outside the singular funnel of the folded node. Hence we do not expect a MMO but a relaxation oscillation.

Whether or not the global return mechanism projects the phase point into the singular funnel can be formalized as follows. Let δ denote the distance from the phase point on $P(L^-)$ of the singular periodic orbit to the strong canard SC with the convention that $\delta > 0$ indicates that the phase point is within the singular funnel. The condition $\delta = 0$ corresponds to the border between MMOs and relaxation oscillations and indicates that the segment of the singular periodic orbit on S_a^+ lies on the strong canard SC. For example, for fixed $g_K = 4$ nS we have $\delta = 0$ for $g_A \approx 0.27$ nS. The δ is a continuous increasing function of g_A, so $\delta < 0$ when $g_A = 0.2$ pS and relaxation oscillations are produced (Fig. 7) and $\delta > 0$ when $g_A = 4$ pS and MMOs are produced (Fig. 8).

The choice of parameter values determines whether or not the singular periodic orbit enters the singular funnel. The behaviors of these singular periodic orbits are summarized in Fig. 10 for the two parameters g_K and g_A. MMOs are predicted for all parameter combinations within the region highlighted in gray. For any value $3.5 < g_k < 6$ nS (and independent of g_A), there exists a folded node singularity on L^+, which is the first requirement for MMOs to exist and explains the left and right boundary of the MMO regime. The second requirement for MMOs, $\delta > 0$, is fulfilled above the

curve $\delta = 0$ which explains the lower boundary of the MMO region. The upper boundary of the MMO region is a curve of saddle-node bifurcations SN_1. Crossing this curve towards increased g_A annihilates the MMO attractor because a stable equilibrium attractor bifurcates. This is a stable hyperpolarized state of the reduced system. There is also a stable depolarized state of the reduced system for $g_K < 3.5$.

5.1 Comparison of bifurcation diagrams

The MMO region in Fig. 10 is very similar to the bursting region in Fig. 3(b) and explains the genesis of the observed bursting region as the singular perturbation parameter C is increased. In both cases the upper bound of the MMO/bursting region is a curve of saddle-node bifurcations SN_1 which indicates that the system is in a hyperpolarized steady state for large conductance g_A. To understand the relation of the left, right and lower boundaries in both bifurcation diagrams in more detail, a bit more canard theory is required, as discussed next.

For sufficiently small values of the perturbation parameter, C in this case, it is possible to calculate the maximal number of small oscillations of a MMO pattern (Wechselberger 2005). This number, s_{max}, depends on the eigenvalues of the linearization of the desingularized system at the FN. Let these eigenvalues be denoted by λ_1 and λ_2, where $|\lambda_1| < |\lambda_2|$, and define the eigenvalue ratio

$$\mu = \frac{\lambda_1}{\lambda_2} \ . \tag{5.10}$$

Then, since at a FN both eigenvalues have the same sign, $0 < \mu < 1$. The maximal number of small oscillations in the MMO is then

$$s_{max} = \left[\frac{\mu + 1}{2\mu} \right] \ , \tag{5.11}$$

the greatest integer less than or equal to $\frac{\mu+1}{2\mu}$. Thus, if s is the number of small oscillations produced in the MMO for sufficiently small C, then $s \leq s_{max}$ where s_{max} is given by Eq. (5.11). Here sufficiently small C means that $\sqrt{\varepsilon} \ll \mu$, where ε is given by Eq. (4.3). Otherwise the system is too far from the singular limit and the bound becomes invalid.

In the present case, μ depends on both g_A and g_K. However, the dependence on g_A is very weak, so that μ changes little if g_K is held fixed and g_A is varied (between the upper and lower bounds of the MMO region). Thus, μ is (almost) constant, and so is s_{max}, along the vertical line segments shown in Fig. 10. When $g_k \approx 3.5$ nS, $\mu = 0$ and for smaller g_K values there are
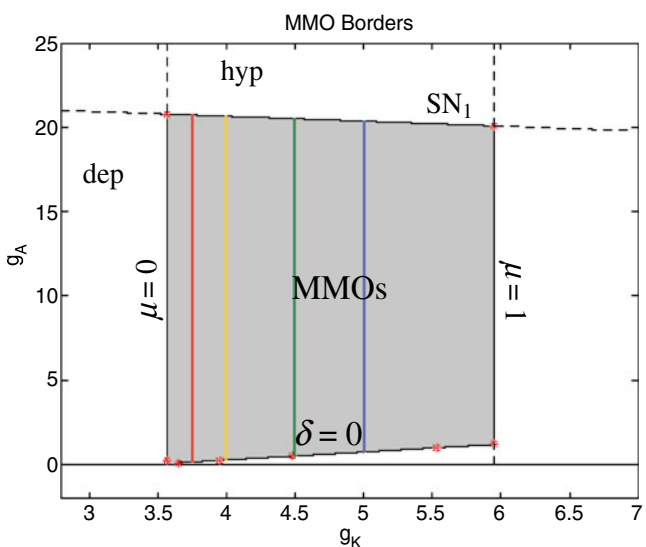
Fig. 10 Region in the g_K-g_A parameter space where MMOs are predicted in the $C \to 0$ limit. The *colored vertical line* segments indicate various values of s_{max}, the maximum number of small oscillations that can occur in an MMO (*red* = 12, *yellow* = 5, *green* = 2, *blue* = 1). This number increases as g_K is decreased

no MMOs. When $g_K \approx 6$ nS, $\mu = 1$ and for larger g_K values there are no MMOs. This explains the notation of the left and right borders in Fig. 10. Near the left border the number of small oscillations in the MMO is large (since $s_{max} \to \infty$ as $\mu \to 0$); near the right border the number of small oscillations is 1 (since $s_{max} \to 1$ as $\mu \to 1$). Note that this is in addition to the initial spike that begins an active phase.

The left border $\mu = 0$ denotes a folded saddle-node (type II) of the reduced flow. To be more precise, we observe a transcritical bifurcation of a folded singularity and an ordinary singularity. To the left of the border we have $\mu < 0$ which corresponds to a folded saddle on L^+, with a stable node equilibrium on S_a^+. If we increase g_K (and therefore μ), this stable equilibrium, the ordinary singularity, merges with the folded singularity for $\mu = 0$ and crosses over to the repelling branch S_r for $\mu > 0$ where it becomes an (unstable) saddle equilibrium. The folded singularity is now a folded node on L^+ which explains the transcritical nature of the folded saddle-node, type II. (A folded saddle-node, type I, corresponds to a true saddle-node bifurcation of two folded singularities of the reduced flow, which we do not observe here.)

Note that the stable node equilibrium for $\mu < 0$ is on the attracting sheet S_a^+. Thus it corresponds to a stable equilibrium of the full system since all three eigenvalues (two from the reduced problem and one from the layer problem) are negative. This corresponds to a stable depolarized state because the delayed rectifier is too weak to repolarize the cell. When g_K is increased so that $\mu > 0$, the equilibrium has bifurcated to the repelling sheet S_r, where it is a saddle point in the reduced system. Hence, it corresponds to an unstable equilibrium of the full system with two positive eigenvalues (one from the reduced problem and one from the layer problem) and one negative eigenvalue (from the reduced problem). Therefore, the real part of two eigenvalues changes sign as the bifurcation point is crossed. Exactly the same happens when $C > 0$, as shown in the bifurcation diagram of Fig. 3. Here we observe a Hopf bifurcation (HP_1), i.e., two (complex conjugate) eigenvalues change their sign. Hence, the singular limit ($C \to 0$) representation of a Hopf bifurcation in a singularly perturbed system is a folded saddle-node, type II, of the corresponding reduced problem. This observation is also confirmed in Fig. 5 where the Hopf bifurcation HP_1 converges to $g_K \approx 3.5$ for $C \to 0$ independent of g_A. Subsequent bifurcations near a folded saddle-node, type II, are currently under investigation with emphasis on the role of the nearby saddle equilibrium on MMO patterns (Guckenheimer 2008; Krupa and Wechselberger 2010).

We next consider the right border, $\mu = 1$, in Fig. 10 and relate it to Fig. 3(b). This border of the MMO regime corresponds for $C = 0$ to a degenerate folded node where two nonzero eigenvalues merge. To the right of this border we have folded foci which possess no canards. Hence we only observe relaxation oscillations as described in Section 3. To the left of the border we have folded nodes with eigenvalue ratio μ close to one which implies that $s_{max} = 1$. Hence we observe MMOs with one extra small-amplitude oscillation (Fig. 11(b)) compared to a relaxation oscillation. In Fig. 3(b) the right border consists of period doubling bifurcations (PD_2). Near the PD_2 bifurcation the phase point in the depolarized state follows the strong canard and alternately jumps up and down, thus producing an oscillation with doubled period (Fig. 11(a)). For smaller g_A values, such as on the lower PD_2 branch, the phase point in the depolarized state travels along the strong canard and jumps down at different locations, creating a period-two relaxation oscillation with slightly different amplitudes. The other period doubling bifurcation (PD_1) in Fig. 3(b) is a transition from single spikes to doublets.

(a)

(b)
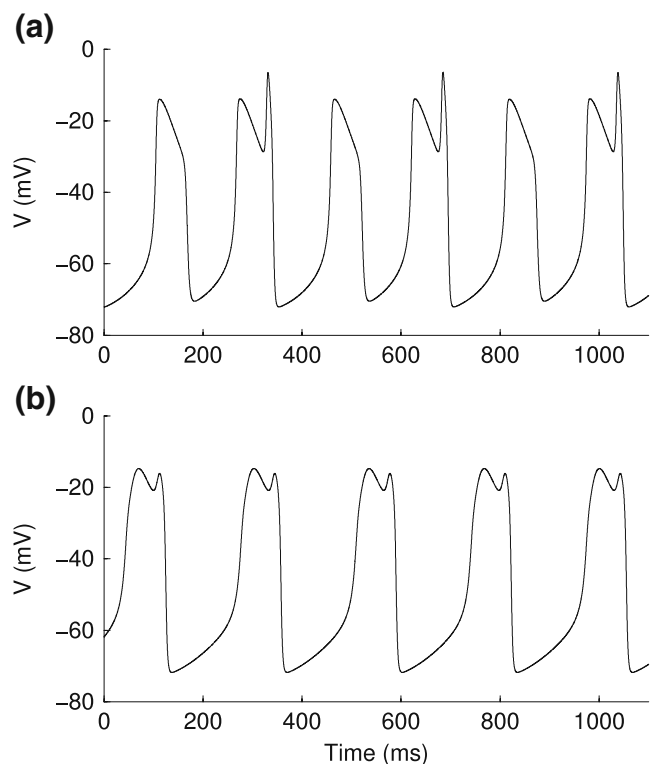
Fig. 11 Time courses of MMO patterns for parameter values $g_A = 10$ nS and $C = 2$ pF near the right PD_2 boundary in Fig. 3: (**a**) a period-doubled oscillation (2^1 MMO pattern) for $g_K = 6.00895$ nS and (**b**) a 1^1 MMO oscillation for $g_K = 5.5$ nS

A last piece of canard theory is required to compare bifurcation structures within the MMO regime in Fig. 10 with Fig. 3(b). For suffciently small values of the perturbation parameter C, there exist $(s_{max} - 1)$ *secondary canards* which partition the funnel region of a folded node into s_{max} subsectors with different rotational properties (Wechselberger 2005). The first subsector is bounded by the strong canard SC and the first secondary canard; trajectories within this subsector make one rotation. The second subsector is bounded by the first and the second secondary canard; trajectories within this subsector make two rotations. The last subsector is bounded by the $(s_{max} - 1)$ secondary canard and the fold curve L^+; trajectories in this last subsector make the maximal s_{max} rotations. Hence, each subsector has a different rotation number.

All secondary canards are within an $O(\varepsilon^{(1-\mu)/2})$ neighborhood of the strong canard SC which implies that the size of the first $(s_{max} - 1)$ subsectors is of $O(\varepsilon^{(1-\mu)/2})$ since they are bordered by secondary canards. The last subsector with maximal rotation number is of size $O(1)$ since it is bordered by the last secondary canard and the fold-curve. In the singular limit, all secondary canards merge with the strong canard and hence only the maximal rotation subsector survives. It follows that if the singular perturbation parameter is sufficiently small compared to the distance $\delta > 0$ of the singular periodic orbit from the SC, i.e., $\delta \gg \varepsilon^{(1-\mu)/2}$ and hence the periodic orbit is within the last subsector, then the observed MMO has maximal rotation number. As δ approaches zero, the periodic orbit moves through all the different rotational sectors, finally reaching the first subsector with only one rotation. Thus, the MMO pattern closest to the border $\delta = 0$ has only one small oscillation.

For parameter values lying on or near the $\delta = 0$ line segment in Fig. 10 the periodic orbit of the singular flow (the concatenation of flow in the reduced system and from the layer problem) enters the singular funnel on or near the SC curve, so for $C > 0$ (but sufficiently small) there will be a single small oscillation associated with the FN. If one increases g_A, moving upward along a vertical line segment in the MMO region of Fig. 10, then the periodic orbit of the singular flow enters further from the SC curve and closer to L^+, so the δ function increases from 0. Therefore, for $C > 0$ the periodic orbit enters the FN through a sector in which s is closer to s_{max} and thus more small oscillations are produced. For example, moving upward along the yellow line segment in Fig. 10 by increasing g_A will result in s increasing from 1 up to 5. For sufficiently small C, this will result in bursting oscillations with 2 spikes (for small g_A) up to 6 spikes (for g_A near the upper bursting boundary).

For $C > 0$, but small, this will result in bursting oscillations with 2 spikes for g_A small up to 6 small oscillations for g_A near the upper bursting boundary.

In summary, the eigenvalue ratio for the FN in the singular system, μ, determines the maximum number of small oscillations (s_{max}) that can occur during the MMO oscillation. This parameter is adjusted through the biophysical parameter g_K. Increasing g_K *decreases* s_{max}. The distance from the strong canard at which the singular periodic orbit enters the singular funnel, δ, determines how close the actual number of small oscillations (s) is to the upper bound s_{max}. This parameter is adjusted through the biophysical parameter g_A. Increasing g_A *increases* s.

Figure 12 shows how the number of spikes in a burst varies for the case $C = 2$ pF, computed through numerical simulation of the full system. To the right and below the bursting region of the g_K-g_A parameter space the system spikes continuously (small blue circles). To the left and above the bursting region the system is at a steady state (blue dots). Within the bursting region, but near the bottom boundary, the number of spikes per burst is small, typically two or three. As one moves away from the lower boundary the number of spikes per burst increases rapidly to a maximum, and the value of this maximum is larger on the left side of the bursting region than on the right side. This is all consistent with
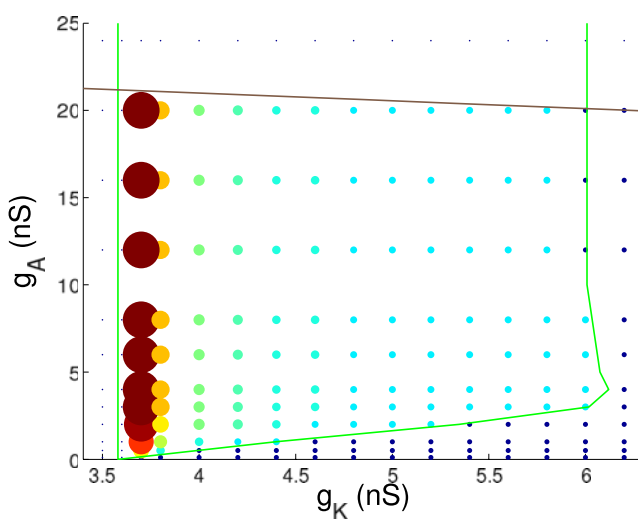
Fig. 12 Number of spikes per burst for a grid of g_K and g_A values ($C = 2$ pF). *Single points* represent steady states, and *small dark circles* represent continuous spiking. *Larger circles with colors* ranging from *light blue* to *red* represent bursting. The larger the *circle*, the greater the number of spikes per burst (same as in Fig 6). The minimum number of spikes is 2 (small, *light blue*), and the maximum is 53 (large, *red*). The *green and brown curves* are the period doubling and saddle node bifurcation curves shown in Fig. 3B

the singular perturbation analysis. Even for larger values of the capacitance C the same trends are observed, however as C is increased the lower bursting boundary moves upward and there is an increase in the range of g_A values over which the number of spikes per burst increases from two to its maximum (not shown).

6 Discussion

Mixed mode oscillations have appeared in several neural applications (Erchova and McGonigle 2008; Wechselberger 2005; Rubin and Wechselberger 2007; Rotstein et al. 2008; Ermentrout and Wechselberger 2009; Drover et al. 2005; Brons et al. 2008; Krupa et al. 2008; Guckenheimer et al. 1997). In this article we have demonstrated how MMOs can produce a type of bursting oscillation (Fig. 1) that has been described in a recent mathematical model of the pituitary lactotroph (Toporikova et al. 2008), and which could potentially describe bursting in other endocrine cells and neurons. We have shown the genesis of this bursting rhythm using geometric singular perturbation theory. The curves in the (g_K, g_A) parameter space that bound the MMO region in the singular limit (Fig. 10) correspond nicely to those that bound the bursting region away from this limit ($C = 2$ pF, Fig. 3). Thus, the analysis performed at the singular limit not only reveals the subtle mechanism of bursting in this system, but it also provides information on the extent of bursting that is consistent with the bifurcation analysis of the full system.

Importantly, the singular perturbation analysis provides information on features that were not apparent from the bifurcation analysis of the full system. While the full-system analysis provided boundaries for the bursting region in parameter space, it did not fully explain the rationale for these boundaries. The singular perturbation analysis gave a clear rationale, in terms of the properties of the folded node singularity and the curves delimiting the singular funnel. Also, singular analysis provided information on how the number of spikes in a burst varies in parameter space. This information could not be obtained from the bifurcation analysis of the full system, but required numerical simulation (Figs. 6 and 12). Finally, the singular theory predicts that the amplitude of the spikes that occur during bursting increase as the square root of the capacitance (the actual value of capacitance for pituitary somatotrophs is ~ 5 pF and for lactotrophs is ~ 6 pF). This dependence of spike amplitude on C can only be obtained from the full system through numerical simulation.

While the singular perturbation analysis has many virtues, it also has limitations. Most obviously, the singular analysis is only guaranteed to be valid for sufficiently small C. Also, the analysis is most effective when there are no more than two slow variables. Thus, the singular analysis has limitations that are not present in the full-system bifurcation analysis. This emphasises the power of combining the two analysis techniques: singular perturbation analysis to understand the oscillation mechanism and extent in parameter space assuming that certain conditions are met, and full-system bifurcation analysis to extend the singular analysis to the non-singular situation that is likely a more accurate description of the biological system.

References

Benoit, E. (1983). Syst'emes lents-rapides dans r3 et leur canards. *Asterisque, 109–110*, 159–191.

Brons, M., Kaper, T. J., & Rotstein, H. G. (2008). Introduction to focus issue: mixed mode oscillations: Experiment, computation, and analysis. *Chaos, 18*, 015101.

Brons, M., Krupa, M., & Wechselberger, M. (2006). Mixed mode oscillations due to the generalized canard phenomenon. *Fields Institute Communications, 49*, 39–63.

Desroches, M., Krauskopf, B., Osinga, H. M. (2008). Mixed-mode oscillations and slow manifolds in the self-coupled FitzHugh–Nagumo system. *Chaos, 18*, 015107.

Drover, J., et al. (2005). Analysis of a canard mechanism by which excitatory synaptic coupling can synchronize neurons at low firing frequencies. *SIAM Journal on Applied Mathematics, 65*, 69–92.

Erchova, I., & McGonigle, D. J. (2008). Rhythms of the brain: An examination of mixed mode oscillation approaches to the analysis of neurophysiological data. *Chaos, 18*, 015115.

Ermentrout, G. B. (2002). *Simulating, analyzing, and animating dynamical systems: A guide to XPPAUT for researchers and students*. Philadelphia: SIAM Books.

Ermentrout, G. B., & Wechselberger, M. (2009). Canards, clusters and synchronization in a weakly coupled interneuron model. *SIAM Journal On Applied Dynamical Systems, 8*, 253–278.

Fenichel, N. (1979). Geometric singular perturbation theory. *Journal of Differential Equations, 31*, 53–98.

Guckenheimer, J. (2008). Singular Hopf bifurcation in systems with two slow variables. *SIAM Journal On Applied Dynamical Systems, 7*, 1355–1377.

Guckenheimer, J., et al. (1997). Bifurcation, bursting, and spike frequency adaptation. *Journal of Computational Neuroscience, 4*, 257–277.

Jones, C. K. R. T. (1995). Geometric singular perturbation theory. In R. Johnson (Ed.), *Dynamical systems. Lecture notes in mathematics* (Vol. 1609, pp. 44–120). New York: Springer.

Kinard, T. A., et al. (1999). Modulation of the bursting properties of single mouse pancreatic β-cells by artificial conductances. *Biophysical Journal, 76*(3), 1423–1435.

Krupa, M., et al. (2008). Mixed-mode oscillations in a three time-scale model for the dopaminergic neuron. *Chaos, 18*, 015106.

Krupa, M., & Wechselberger, M. (2010). Local analysis near a folded saddle-node singularity. *Journal of Differential Equations*. doi:10.1016/j.jde.2010.02.006.

Kuryshev, Y. A., Childs, G. V., & Ritchie, A. K. (1996). Corticotropin-releasing hormone stimulates Ca^{2+} entry through L- and P-type Ca^{2+} channels in rat corticotropes. *Endocrinology, 137*, 2269–2277.

LeBeau, A. P., et al. (1998). Analysis of a reduced model of corticotroph action potentials. *Journal of Theoretical Biology, 192*, 319–339.

Morris, C., & Lecar, H. (1981). Voltage oscillations in the barnacle giant muscle fiber. *Biophysical Journal, 35*, 193–213.

Rinzel, J. (1987). A formal classification of bursting mechanisms in excitable systems. In E. Teramoto, & M. Yamaguti (Eds.), *Mathematical topics in population biology, morphogenesis and neurosciences. Lecture notes in biomathematics* (Vol. 71, pp. 267–281). Berlin: Springer.

Rinzel, J., & Ermentrout, G. B. (1998). Analysis of neural excitability and oscillations. In C. Koch, & I. Segev (Eds.), *Methods in neuronal modeling: From synapses to networks* (2nd ed., pp. 251–292). Cambridge: MIT.

Rotstein, H., Wechselberger, M., & Kopell, N. (2008). Canard induced mixed-mode oscillations in a medial entorhinal cortex layer II stellate cell model. *SIAM Journal of Dynamic Systems, 7*, 1582–1611.

Rubin, J., & Wechselberger, M. (2007). Giant squid-hidden canard: The 3D geometry of the Hodgkin–Huxley model. *Biological Cybernetics, 97*, 5–32.

Shorten, P. R., et al. (2000). CRH-induced electrical activity and calcium signalling in pituitary corticotrophs. *Journal of Theoretical Biology, 206*, 395–405.

Stern, J. V. (2008). Resetting behavior in a model of bursting in secretory pituitary cells: Distinguishing plateaus from pseudo-plateaus. *Bulletin of Mathematical Biology, 70*, 68–88.

Szmolyan, P., & Wechselberger, M. (2001). Canards in $\mathbb{R}^3$. *Journal of Differential Equations, 177*, 419–453.

Szmolyan, P., & Wechselberger, M. (2004). Relaxation oscillations in $\mathbb{R}^3$. *Journal of Differential Equations, 200*, 69–104.

Tabak, J., et al. (2007). Low dose of dopamine may stimulate prolactin secretion by increasing fast potassium currents. *Journal of Computational Neuroscience, 22*, 211–222.

Toporikova, N., et al. (2008). A-type K^+ current can act as a trigger for bursting in the absence of a slow variable. *Neural Computation, 20*, 436–451.

Tsaneva-Atanasova, K., et al. (2007). Mechanism of spontaneous and receptor-controlled electrical activity in pituitary somatotrophs: Experiments and theory. *Journal of Neurophysiology, 98*, 131–144.

Van Goor, F. V., et al. (2001). Dependence of pituitary hormone secretion on the pattern of spontaneous voltage-gated calcium influx. *Journal of Biological Chemistry, 276*, 33840–33846.

Wechselberger, M., (2005). Existence and bifurcation of canards in $\mathbb{R}^3$ in the case of a folded node. *SIAM Journal of Dynamic Systems, 4*, 101–139.

Zhang, M., et al. (2003). The Ca^{2+} dynamics of isolated mouse β-cells and islets: Implications for mathematical models. *Biophysical Journal, 84*, 2852–2870.